PERGAMON

Computers & Fluids 31 (2002) 911–934

computers & fluids

www.elsevier.com/locate/compfluid

Flow topology in a steady three-dimensional lid-driven cavity

T.W.H. Sheu *, S.F. Tsai

Department of Engineering Science and Ocean Engineering, National Taiwan University, 73, Chou-Shan Road, Taipei 106, Taiwan, ROC

Received 11 July 2000; received in revised form 28 June 2001

Abstract

We present in this paper a thorough investigation of three-dimensional flow in a cubical cavity, subject to a constant velocity lid on its roof. In this steady-state analysis, we adopt the mixed formulation on tri-quadratic elements to preserve mass conservation. To resolve difficulties in the asymmetric and indefinite large-size matrix equations, we apply the BiCGSTAB solution solver. To achieve stability, weighting functions are designed in favor of variables on the upstream side. To achieve accuracy, the weighting functions are properly chosen so that false diffusion errors can be largely suppressed by the equipped streamline operator. Our aim is to gain some physical insight into the vortical flow using a theoretically rigorous topological theory. To broaden our understanding of the vortex dynamics in the cavity, we also study in detail the longitudinal spiralling motion in the flow interior.

Keywords: Three-dimensional; BiCGSTAB solution solver; Topological theory

1. Introduction

Among the few selected geometries that have been studied in detail is cavity flow driven by a roof lid. Despite its simple geometry, flow in this cavity exhibits features of more complex geometry flows. This problem, thus, is a good test for experimental flow research [1–8]. Another reason for the proliferation of research on this flow is that the problem under investigation is intended to test the accuracy of numerical methods so far developed for the prediction of incompressible Navier–Stokes fluid flows. Thus, extensive numerical studies on this problem have been carried out.

* Corresponding author. Address: Department of Engineering Science and Ocean Engineering, 73, Chou-Shan Road, Taipei, Taiwan, ROC. Tel.: +886-2-23625-470; fax: +886-2-392-9885/23661703.

E-mail address: sheu@ACCS.na.ntu.edu.tw (T.W.H. Sheu).

0045-7930/02/$ - see front matter
PII: S0045-7930(01)00083-4

Experimental studies on the lid-driven cavity problem started in the early 1980s. In these studies, Taylor–Görtler-like (TGL) vortices were experimentally observed by Koseff et al. [3]. Koseff and Street [4] observed corner vortices in the vicinity of the two vertical end walls and local TGL vortices over the span of the cavity with spanwise aspect ratio (SAR) values of ($\equiv$ L:B $= 1, 2, 3$). In the case of $Re \sim 3000$, eight pairs of TGL vortices have been observed. On increasing Reynolds number Re up to 6000, another three pairs of TGL vortices become visible. For Reynolds numbers as high as 6000–8000, unsteady flow can no longer be sustained; thus, it evolves into turbulence. For a comprehensive literature review, see the research work of Street and his colleagues [3–6,9–13].

Numerical investigation into this problem dates back to the pioneer work of Burggraf [14]. While some fundamental flow phenomena have been revealed through two-dimensional solutions, many of the subtleties of third dimensionality are missing. The recent progress in numerical analysis and computer hardware has made it possible to analyze unsteady flow problems by solving their corresponding Navier–Stokes equations with a large number of grid points within a three-dimensional domain. The interested reader can refer to Ref. [15] who recently provided an excellent review of this subject. In 1985, TGL vortices were first numerically confirmed by Freitas et al. [10]. Six years later, the GAMM-committee sponsored a workshop dedicated to numerical simulation of a lid-driven cavity flow at $Re = 3200$ for SAR $= 3{:}1$ [16] with the aim of ascertaining the number of TGL vortex pairs appearing in the transverse direction. Comparisons were also made among the participants, and it was surprising to find that the conclusions drawn were quite different among the contributors. They differed in their opinions not only on the flow symmetry, but also on the number of TGL vortex pairs. In this light, we felt that much work remains to be done, thus prompting our study of the lid-driven cavity problem over the last five years.

Numerical exploration into flow instability caused by longitudinal vortices has been the subject of our previous efforts [17–21]. These studies have helped explain why spiralling vortices inside the upstream secondary eddy tend to destabilize the flow by means of laminar instabilities. After years of exploration into this problem, there are very few, if any, theoretical investigations of vortical flow structure in the cavity. The present work is a continuation of our previous research endeavors aimed at presenting a clear picture of the vortices by using a theoretically rigorous topology theory [22–24]. It is hoped that this topological description of vorticity can provide insight into longitudinal vortical flow.

Investigation into incompressible viscous flow problems can be conducted using pressure-based methods or mixed formulations [25]. The difficult task in the pressure-based approach is to implement proper pressure boundary conditions. Thus, we will confine ourselves to the mixed formulation, which solves the continuity equation directly rather than solving the Poisson equation for the pressure in order to eliminate ambiguity in the implementation of proper boundary conditions for the pressure [25]. In the mixed formulation, difficulties also arise as to the choice of finite element spaces for working variables and the choice of iterative solvers for solving indefinite and unsymmetric matrix equations. To solve the first problem, we consider an element which retains the $\mathscr{LBB}$ (Ladyzhenskaya–Babuška–Brezzi) stability condition [26,27]. In the finite element calculation of large-size matrix equations, one has no choice but to employ the parallelized iterative solver to resolve difficulties in matrix indefiniteness and asymmetry [28].

The organization of the rest of this paper is as follows. In Section 2, we present the working Navier–Stokes equations and the divergence-free constraint condition to preserve conservation of

momenta and mass. In order to make these equations well posed, boundary conditions are prescribed along the entire boundary. This is followed by a brief outline of the Petrov–Galerkin finite element model. The BiCGSTAB iterative solution solver [29], which can effectively resolve difficulties with indefinity and asymmetry, is also given. In Section 4, we describe the physical problem under investigation and present results using the topological theory [22–24] to reveal the flow structure. In Section 5, we make concluding remarks on the implications of the reported results.

2. Numerical model

Computational modeling of lid-driven cavity flow requires solving three-dimensional flow equations. Under the incompressible and steady assumptions, the continuity and Navier–Stokes equations in Cartesian coordinates are as follows:

$$\frac{\partial u_i}{\partial x_i} = 0, \tag{1}$$

$$\frac{\partial}{\partial x_m}(u_m u_i) = -\frac{\partial p}{\partial x_i} + \frac{1}{Re}\frac{\partial^2 u_i}{\partial x_m \partial x_m}. \tag{2}$$

The above elliptic differential system for the velocity field $\underline{u}$ and pressure p is subject to the Dirichlet type boundary condition given by $\underline{u} = \underline{g}$, where

$$\int_\Gamma \underline{n} \cdot \underline{g}\, \mathrm{d}\Gamma = 0. \tag{3}$$

The rationale behind choosing the primitive-variable setting is that closure boundary conditions are clearly defined [30]. More importantly, these closure conditions are relatively easy to implement for the confined flow simulation. For purposes of generality, the primitive-variable differential system has been further normalized. In this study, all lengths have been scaled by the cavity height l_{ref}, the velocity components u_{ref} by the lid velocity applied on the cavity roof. The Reynolds number is, thus, defined as $Re = u_{\mathrm{ref}} l_{\mathrm{ref}}/v$, where v is known as the kinematic viscosity of the fluid flow. The assumption made in this study is that the flow is laminar; turbulence modeling is left for future investigation.

Solutions to Eqs. (1) and (2) are obtained in the weak sense based on the following weighted residuals statement: Given admissive functions $\underline{w} \in \mathscr{H}^1_0(\Omega) \times \mathscr{H}^1_0(\Omega)$ and $q \in \mathscr{L}^2_0(\Omega)$, primitive variables defined in a simply connected domain Ω are subject to the essential-type boundary condition $\underline{u} = \underline{g}$ on $\partial\Omega \equiv \Gamma$, and we seek $\underline{u} \in \mathscr{H}^1_0(\Omega)$ and $p \in \mathscr{L}^2_0(\Omega)$ from

$$\begin{aligned}\int_\Omega (\underline{u}\cdot\nabla)\underline{u}\cdot\underline{w}\,\mathrm{d}\Omega + \frac{1}{Re}\int_\Omega \nabla\underline{u} : \nabla\underline{w}\,\mathrm{d}\Omega - \int_\Omega p\nabla\cdot\underline{w}\,\mathrm{d}\Omega \\ = \int_{\Gamma/\Gamma_n} r\underline{w}\cdot\underline{n}\,\mathrm{d}\Gamma + \int_{\Gamma/\Gamma_\gamma} \underline{s}\cdot\underline{w}\times\underline{n}\,\mathrm{d}\Gamma,\end{aligned} \tag{4}$$

$$\int_\Omega (\nabla\cdot\underline{u})\, q\,\mathrm{d}\Omega = 0. \tag{5}$$

In Eq. (4), $\Gamma/\Gamma_{n,r}$ denotes the complement of $\Gamma_{n,r}$ in $\Gamma = \partial\Omega$. By definition, $\underline{\phi} \in \Gamma/\Gamma_i$ $(i = n, r)$ implies that $\underline{\phi} \in \Gamma$ but that $\underline{\phi} \notin \Gamma_i$. We denote $\underline{n}$ as the unit outward normal vector to Γ. In Eq. (4), $r = -p + (1/Re)\,\underline{n} \cdot \nabla\underline{u} \cdot \underline{n}$ and $\underline{s} = (1/Re)\,\underline{n} \cdot \nabla\underline{u} \times \underline{n}$.

Basis spaces chosen for storing primitive variables are critical to success with the mixed finite element simulation of incompressible fluid flow equations. The $\mathscr{LBB}$ (or *inf–sup*) condition is the guiding principle in choosing basis spaces for primitive variables [26,27]. The element considered here is schematically shown in Fig. 1 and has been shown to accommodate the inf–sup div-stability condition. This chosen element involves tri-quadratic polynomials, N^i $(i = 1\text{–}27)$, for the velocities and tri-linear polynomials, M^i $(i = 1\text{–}8)$, for the pressure.

Prediction of high Reynolds number flows requires careful treatment of advective terms. Enhancement of stability can be accomplished through the addition of a biased polynomial to the shape function [31]. As a result, information at the upwind side is favorably considered. Upwind schemes are, however, prone to numerical contamination due to the introduction of false diffusion errors [32], which are typical of multi-dimensional analyses. To avoid this type of prediction error without sacrificing stability, we have applied our previously developed streamline operator on quadratic elements so that the stabilizing terms are mainly added along the primary flow direction to improve the discrete stability [28].

In the mixed finite element context, we are usually faced with very large-size matrix equations. Employment of Gaussian-elimination-like direct solvers can consume a great deal of computer time, and the storage requirement can greatly exceed the capacity of today's computers. For this reason, iterative solvers need to be used to circumvent this problem. In this study, we apply the BiCGSTAB iterative solver [29]. This solver was developed within the Lanczos framework to solve unsymmetric matrix equations without sacrificing irregular convergence. The choice of BiCGSTAB to solve the presently encountered unsymmetric and indefinite matrix equations is

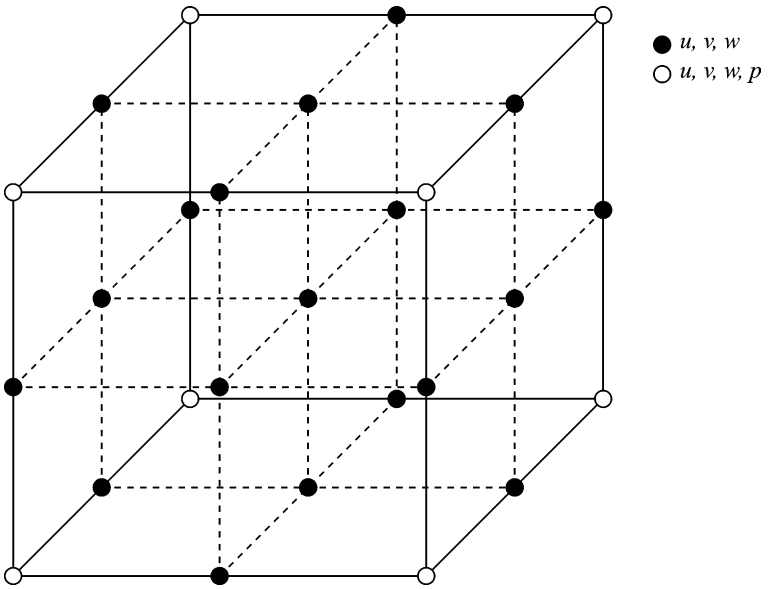

Fig. 1. The variable layout in the tri-quadratic finite element.

owing to its accommodation of local minimization of residuals through GMRES (1). Another advantage of applying BiCGSTAB is that mathematical manipulation of the transpose matrix is avoided. Nevertheless, it is important to prevent pivoting breakdown [33] and Lanczos breakdown because the BiCGSTAB method still inherits the essence of BiCG [34]. For computational efficiency, we have integrated the element-by-element capability into the BiCGSTAB solver. The reader is referred to Ref. [35] for additional details about the EBE–BiCGSTAB solution algorithm applied here.

3. Problem description and validation

The problem under investigation is schematically shown in Fig. 2. The cavity has a depth-to-width aspect ratio of 1:1 and a span-to-width aspect ratio of 1:1. Problems with other length ratios and Reynolds numbers have been studied elsewhere. The reader can refer to our previous publications [17–21]. For an intensive discussion of the flow details, we discuss results for $Re = 400$. This Reynolds number is not high in the sense that TGL vortices are not seen in the cavity, thus permitting steady-state flow analysis. The present analysis was conducted on the whole cavity without assuming flow symmetry. Pitchfork bifurcation, if any exists, then can be detected. To resolve the flow details, grid points shown in Fig. 2 are clustered in regions immediately adjacent to the solid wall as well as in the vicinity of the cavity roof. This implies that the cavity has been non-uniformly discretized, resulting in a mesh having a resolution of 41^3 and 51^3 nodes in the x, y, z directions, respectively.

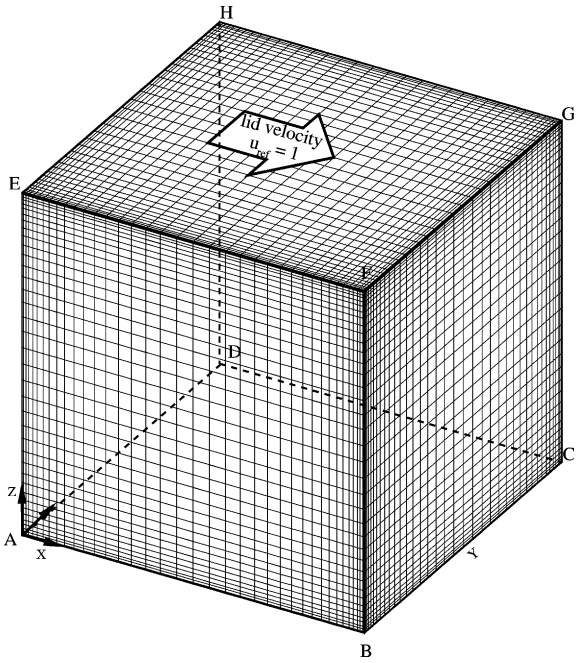

Fig. 2. Grid layout and geometric description (ABCD: bottom plane; EFGH: upper lid plane; EABF and HDCG: vertical end walls; EADH: upstream side wall; FBCG: downstream side wall).

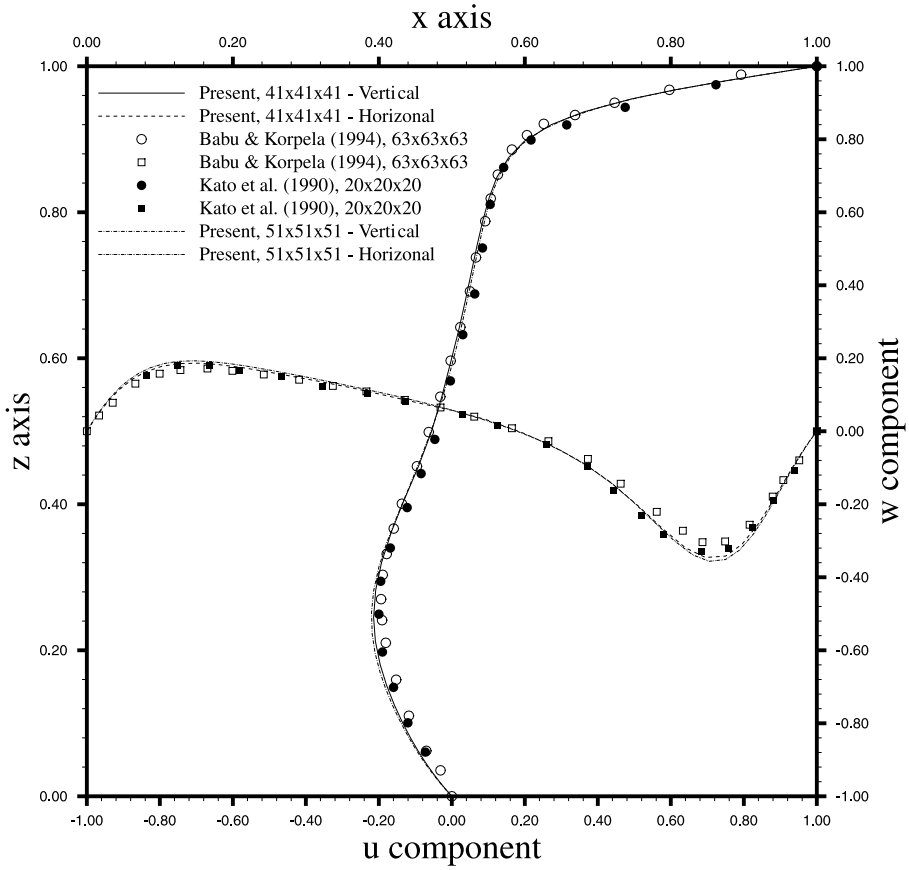

Fig. 3. Comparison of u and w velocity profiles at the plane of symmetry $y = 0.5$.

As a means of checking the integrity of the three-dimensional Petrov–Galerkin finite element code used to investigate incompressible flow equations, we validate the code first for the problem having benchmark test data. Analysis was carried out in a cubical cavity of unit length for the case with $Re = 400$. The calculation results show the good agreement with the data of Babu and Korpela [36] and Kato et al. [37] shown in Fig. 3, which plots velocity profiles along the vertical and horizontal centerlines on the mid-plane of the cavity. Since grid-independent solutions are revealed, discussion of results is based on the solutions obtained at 41^3 nodes.

4. Results and discussion

4.1. Flow topology on the solid surface

The first step in exploring vortical details in a cavity is to extract physically meaningful data from the enormous amount of the three-dimensional data. In this study, topological theory was chosen so as to obtain a better understanding of three-dimensional features of the vortical flow in

the lid-driven cavity. Among the methods which enable exploration of kinematics of three-dimensional fluid flows, one can conduct a topological study of limiting streamlines (or wall streamlines) [22] or skin-friction lines [24]. In addition to these vector quantities, a graphical visualization of a scalar quantity, such as the density of helicity or its normalized value, can be used to achieve this goal [23]. We consider limiting streamlines in the topological study of the flow kinematics. Limiting streamlines are, by definition, streamlines immediately above the wall surface. The projection of the three-dimensional limiting streamlines onto a no-slip wall is computationally analogous to experimental surface flow visualization.

Fig. 4 plots a three-dimensional view of limiting streamlines on five solid surfaces. It is remarkable that the kinematic aspect of these limiting streamlines are featured by some points that are distinct in nature. Using the terminology of Legendre [22], they are called either singular or critical points. In light of the distinct nature of these critical points, attention should be paid to them to gain a better understanding of kinematically possible cavity flow driven by a roof lid. For descriptive purposes, the wall plane, schematically shown in Fig. 5, is assumed to be a no-slip plane $z^* = 0$. By definition, streamlines are integral representations of the curves $\mathrm{d}\underline{x}^*/\mathrm{d}t = \underline{u}^*$, where $\mathrm{d}\underline{x}^*$ is the direction of the streamline and $\underline{u}^*$ is the instantaneous velocity vector. By

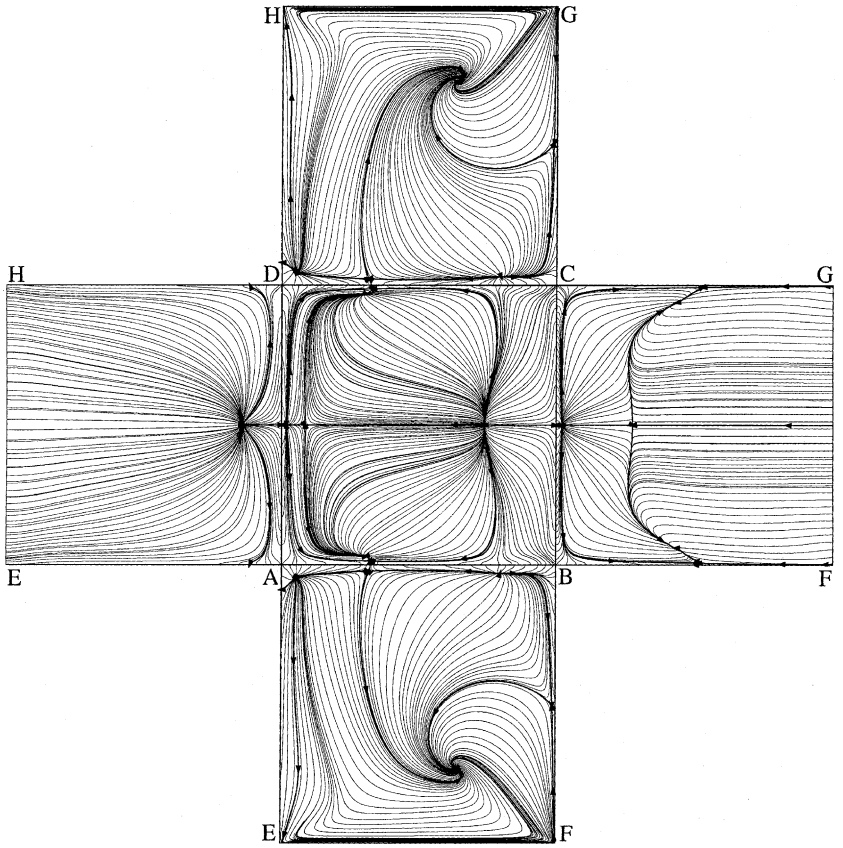

Fig. 4. Limiting streamlines plotted on five solid walls of the cavity.

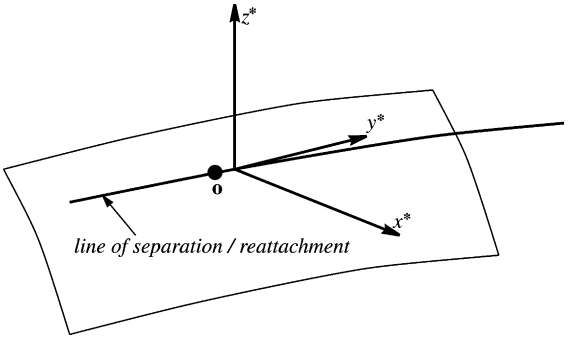

Fig. 5. An arbitrary plane with its outward normal in the direction z^*.

linearizing equation $\mathrm{d}\underline{x}^*/\mathrm{d}t = \underline{u}^*$ around an arbitrary point $\underline{x}_0^*$, we can have $\mathrm{d}\underline{x}^*/\mathrm{d}t = (\underline{\underline{A}}\,\underline{x}^* + \underline{b})z^*$ in the limiting case of $z^* \to 0$. Here, $\underline{b}$ is a constant vector and $\underline{\underline{A}} = [\partial \underline{u}^*/\partial \underline{x}^*]_{\underline{x}^* = \underline{x}_0^*}$. By definition, the magnitude of $\underline{u}^*$ is zero; therefore, its direction is indeterminate. This enables us to determine the critical point as $\underline{x}_c^* = -\underline{\underline{A}}^{-1}\,\underline{b}$.

Flows behaviors immediately adjacent to the so-called critical point are characterized by the eigenvectors and eigenvalues of the Jacobian matrix $|\partial \underline{u}^*/\partial \underline{x}^*|$. Singular points can be classified as nodal (N) and saddle (S) points. Nodal points can be further divided into nodes and foci (or spiral nodes). A real eigenvector with a negative eigenvalue points towards a critical point. In contrast, an eigenvector in association with a positive eigenvalue is repelled from the critical point. If complex eigenvectors are computed, limiting streamlines either spiral towards or are repelled spirally from the critical point, depending on the signs of the two real parts of eigenvalues λ_1 (real) and $\lambda_2 \pm \mathrm{i}\lambda_3$ (conjugate complex).

According to the eigenvalues of $[\partial \underline{u}^*/\partial \underline{x}^*]$, we can determine not only the singular points, but also their classification. To give an impression of the surface-flow pattern, we provide in Fig. 6 a sketch of the critical points. Also shown in this figure is the classification of these points. As a means of checking whether all the critical points determined by the above eigenvalue analysis of $[\partial \underline{u}^*/\partial \underline{x}^*]$ are kinematically possible, we follow the topological rule of Davey [38] and Lighthill [24]. Summing the critical points reveals that $\sum S = 10$ and $\sum N = 12$ on the cavity surfaces. This confirms the validity of the present three-dimensional calculation since the computed numbers of the nodes N and saddles S satisfy

$$\sum N = \sum S + 2. \tag{6}$$

All the surface topological points are tabulated in the Table 1 for the reader's reference.

An examination of the limiting streamlines shown in Fig. 4 and the critical points shown in Fig. 6 leads to the following observations. At a critical point, all of the limiting streamlines are directed towards or away from the node. At a node of separation, say point (1.000000, 0.063216, 0.434984) (point #4 shown in Figs. 6 and 7), all of the nearby limiting streamlines are directed towards the node. If the limiting streamlines spiral into or out of a node, we call this node, namely points $\otimes$ shown in Fig. 7, a focus. A focal point into which nearby limiting streamlines are directed is called a spiral point of detachment or separation. In contrast, a critical point whose

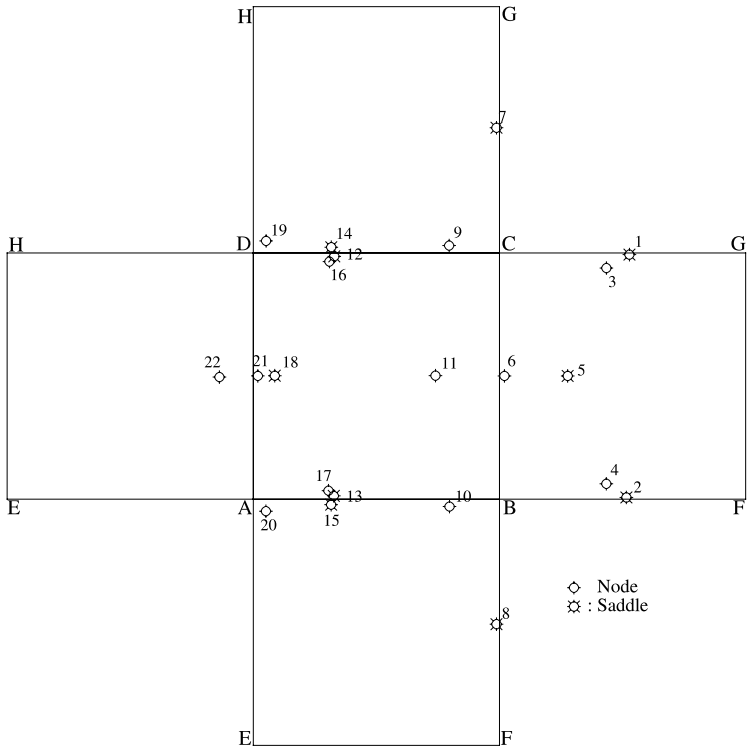

Fig. 6. A plot of critical points of different classification on five solid walls of the cavity.

adjacent limiting streamlines are directed outwards is called a point of reattachment. Two particular lines, called separatrices, are observed to pass through the saddle point. The direction on either side of the singular point is inward on one particular line and outward on the other line.

From the wall-streamlines shown in Fig. 4, it is clear that several families of limiting streamlines are directed either towards or away from the computed singular points. To see how the lines of separation and reattachment are determined, consider the plane shown in Fig. 5. According to Zhang [39], at a point "o" located on an arbitrary line of separation the following three conditions hold:

$$\left.\frac{\partial u}{\partial z^*}\right|_0 < 0,$$
$$\left.\frac{\partial^2 u}{\partial x^* \partial z^*}\right|_0 < 0, \tag{7}$$
$$\left.\frac{\partial^2 w}{\partial z^{*2}}\right|_0 > 0.$$

By virtue of the above conditions and the no-slip condition, the velocities u, v, w are expanded with respect to their values computed at "o". These velocities are expressed in terms of z^* as

Table 1
Spatial locations of singular points

Number	Type	Physical coordinate
1	Saddle	(1.000000, 0.990002, 0.518093)
2	Saddle	(1.000000, 0.009998, 0.518093)
3	Attracting-Node	(1.000000, 0.936784, 0.434984)
4	Attracting-Node	(1.000000, 0.063216, 0.434984)
5	Saddle	(1.000000, 0.500000, 0.278292)
6	Repelling-Node	(1.000000, 0.500000, 0.022669)
7	Saddle	(0.985353, 1.000000, 0.506517)
8	Saddle	(0.985353, 0.000000, 0.506517)
9	Repelling-Node	(0.795412, 1.000000, 0.032967)
10	Repelling-Node	(0.795412, 0.000000, 0.032967)
11	Repelling-Node	(0.737776, 0.500000, 0.000000)
12	Saddle	(0.328579, 0.983235, 0.000000)
13	Saddle	(0.328579, 0.016765, 0.000000)
14	Saddle	(0.316996, 1.000000, 0.026026)
15	Saddle	(0.316996, 0.000000, 0.026026)
16	Attracting-Node	(0.309044, 0.966091, 0.000000)
17	Attracting-Node	(0.309044, 0.033909, 0.000000)
18	Saddle	(0.088356, 0.500000, 0.000000)
19	Repelling-Node	(0.053676, 1.000000, 0.051789)
20	Repelling-Node	(0.053676, 0.000000, 0.051789)
21	Repelling-Node	(0.019895, 0.500000, 0.000000)
22	Repelling-Node	(0.000000, 0.500000, 0.144760)

$$
\begin{aligned}
u &= \frac{1}{2}\frac{\partial^2 u}{\partial z^{*2}}\bigg|_0 z^{*2} + \cdots + \frac{\partial^2 u}{\partial x^* \partial z^*}\bigg|_0 x^* z^* + \cdots,\\
v &= \frac{\partial v}{\partial z^*}\bigg|_0 z^* + \frac{1}{2}\frac{\partial^2 v}{\partial z^{*2}}\bigg|_0 z^{*2} + \cdots + \frac{\partial^2 v}{\partial x^* \partial z^*}\bigg|_0 x^* z^* + \frac{\partial^2 v}{\partial y^* \partial z^*}\bigg|_0 y^* z^* + \cdots,\\
w &= \frac{\partial w}{\partial z^*}\bigg|_0 z^* + \frac{1}{2}\frac{\partial^2 w}{\partial z^{*2}}\bigg|_0 z^{*2} + \cdots.
\end{aligned}
\tag{8}
$$

The limiting streamline on the $z^* = 0$ plane is given below in the case of $z^* \to 0$:

$$
\frac{\mathrm{d}x^*}{\mathrm{d}y^*} = \frac{u}{v} \approx \frac{(\partial^2 u/\partial x^* \partial z^*)|_0 x^*}{(\partial v/\partial z^*)|_0 + (\partial^2 v/\partial x^* \partial z^*)|_0 x^* + (\partial^2 v/\partial y^* \partial z^*)|_0 y^*}. \tag{9}
$$

Based on the above equation defining the line of separation, we determined them on the theoretical basis and plot them in Fig. 7 to give the reader a global view of flow separations near the cavity wall.

A close examination on the lines of separation reveals that they have one feature in common. Lines of separation are found to have origins in the saddle point and to terminate either at a spiral node in the flow interior or at the half-node located on the intersection line of two adjacent walls. These findings prompt us to give a theoretical demonstration of their existence. The reader is

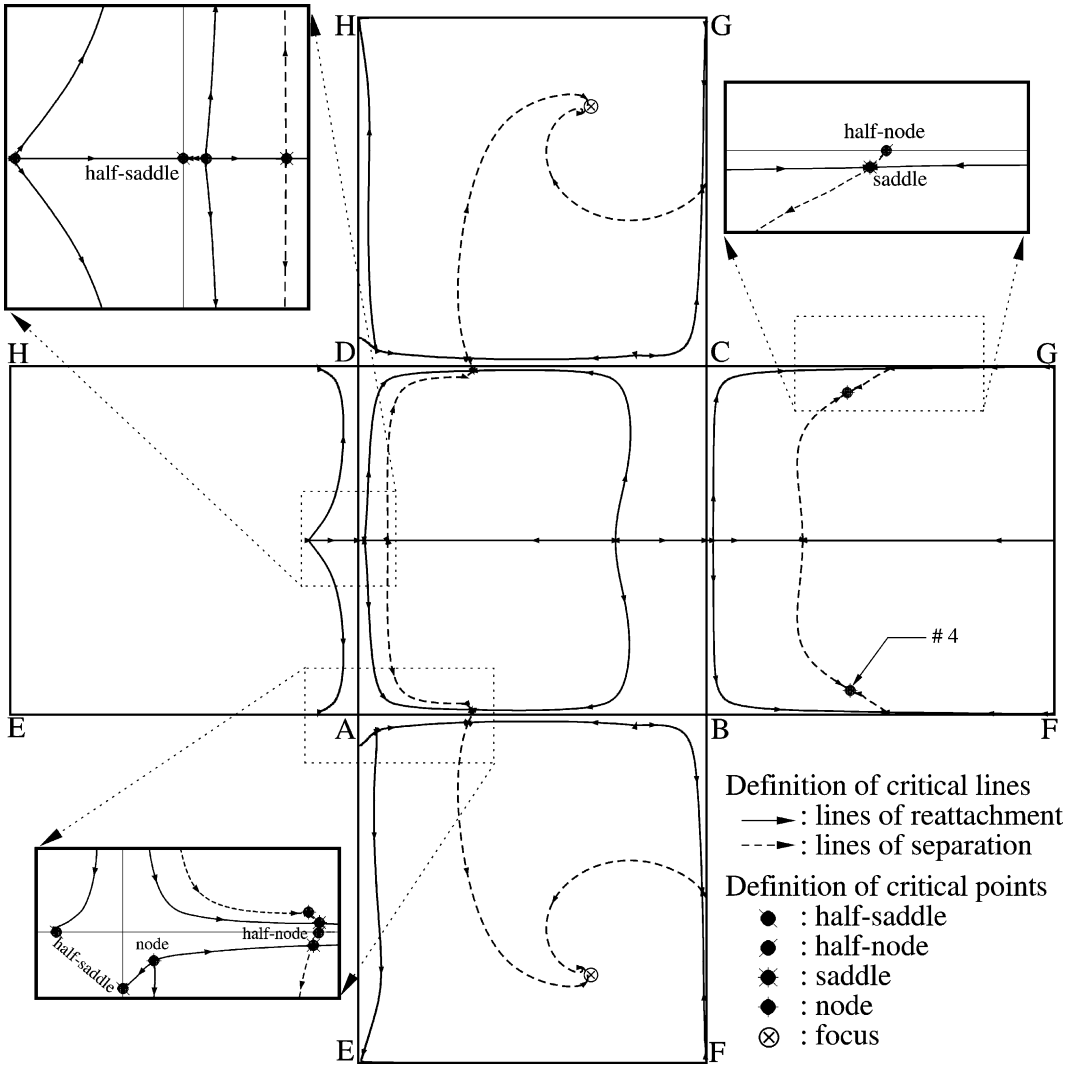

Fig. 7. Lines of separation and reattachment on the five solid walls of the cavity.

referred to the proof, given in Appendix A, following in the same vein as Zhang and Deng [40]. The line of separation with a saddle as a starting point was first recognized by Lighthill [24] and is referred to as close-type separation.

Another remarkable finding from the plotted line of separation is that more than one singular point is seen on this line. Clearly revealed by Fig. 7 is that on the lines of separation saddle and node appear in an alternating fashion. The theoretical support for this observation was given by Zhang and Deng [40]. In regions near the two intersecting planes, lines of separation have a saddle-half node-saddle configuration. The half-node is exactly located at the line of two intersecting planes. In the present study, a line of separation starting at a regular point was not

observed. Such a separation is featured by $\partial v/\partial z^* \neq 0$ at point "o" and is regarded as open-type separation, as first explained by Wang [41].

Unlike lines of separation, wall-streamlines adjacent to the line of reattachment are repelled from this line. For completeness, we also plot lines of reattachment on the five cavity walls in Fig. 7. This figure gives an impression of the typical surface topology of this particular reattachment phenomenon. Specific to the lines of reattachment is that they emanate from a node and terminate at a saddle. Near the two intersecting planes, lines of reattachment have two nodes, in between which there is a half-saddle.

4.2. Vortical flow pattern in the vicinity of the vortical coreline

To get additional insight into vortical flow driven by a roof lid, we will now proceed to study the flow on planes which are locally orthogonal to the vortical coreline. On the plane with a unit normal vector $\underline{n}$, schematically shown in Fig. 8, two coordinates t_1 and t_2 are perpendicular to each other, and are all orthogonal to $\underline{n}$. Streamlines on the t_1–t_2 plane are, by definition, obtained as $\mathrm{d}t_1/\mathrm{d}t_2 = u_{t_1}/u_{t_2}$. Given this definition, we can now proceed to a more theoretical discussion of the vortex established in the cubical cavity. Let us find first the vortical coreline, which is regarded as the main signature of the vortical flow. The vortical coreline is the collection of spatial locations, at which points u_{t_1} and u_{t_2} on a plane with an outward normal n have values of zero. Sketching the vortical coreline, as shown in Fig. 9, is, thus, quite a delicate task. Spatial coordinates that span the vortical coreline are tabulated in Table 2 for the reader's reference. Upon determining the vortical coreline, we computed the velocity component along the vortical coreline and plot its distribution against y in Fig. 10(a). Along the vortical coreline, we then calculated $\lambda \equiv (\partial u_n/\partial n)$ and plotted them against y in Fig. 10(b). In one half of the cavity, there is an increasing value of λ, followed by a decreasing value of λ in the direction towards the plane of symmetry $y = 0.5$. Results exhibiting the change of λ ($\equiv \partial u_n/\partial n$) inspire us

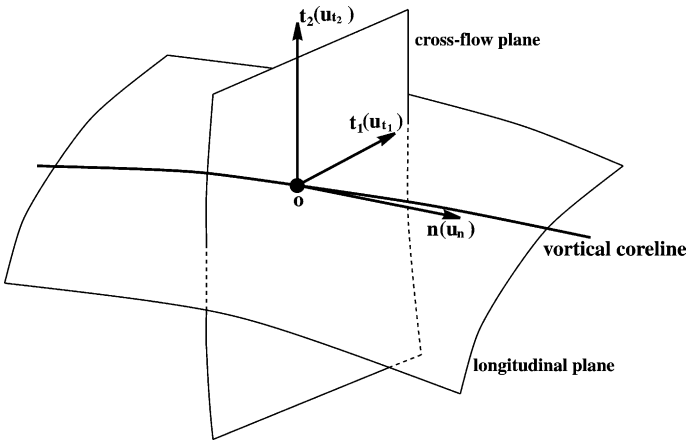

Fig. 8. An illustration of a plane, which is locally normal to the vortical coreline, and the longitudinal plane.

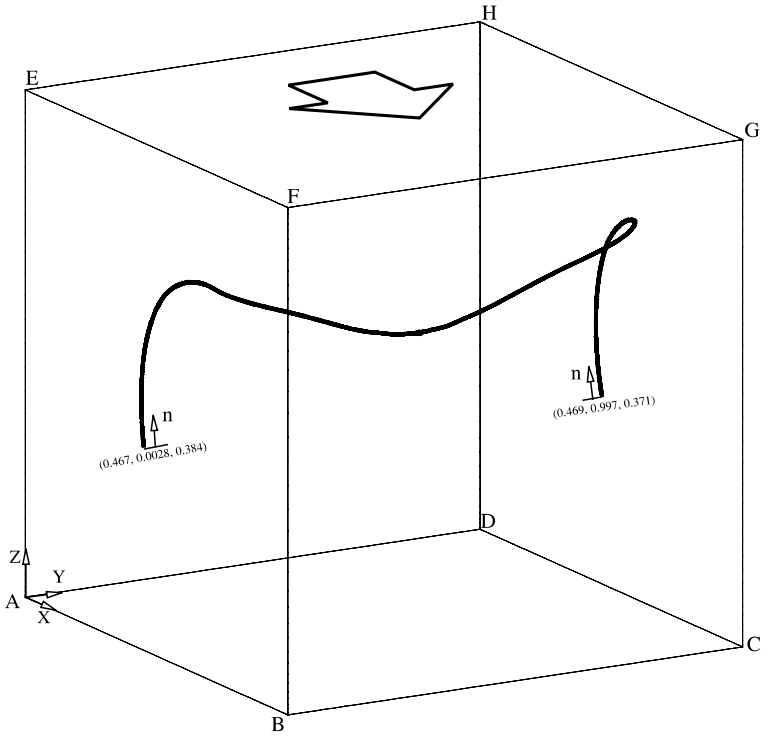

Fig. 9. The computed vortical coreline in the driven cavity.

Table 2
Spatial coordinates of the computed vortical coreline

x	*y*	*z*
4.360812306E−01	3.419186687E−03	4.957499802E−01
4.509942532E−01	4.719771910E−03	6.042528152E−01
4.960576296E−01	7.333191577E−03	6.914645433E−01
5.712176561E−01	1.324093528E−02	7.482188940E−01
6.519504786E−01	3.793755919E−02	7.542282343E−01
6.548249125E−01	1.259413064E−01	7.125176191E−01
6.432981491E−01	2.331477702E−01	6.739135385E−01
6.349019408E−01	3.420910835E−01	6.322959065E−01
6.339827776E−01	4.615832269E−01	6.035609245E−01
6.342189908E−01	5.000000000E−01	6.010810137E−01
6.338430047E−01	5.471287370E−01	6.044864058E−01
6.348633170E−01	6.675446630E−01	6.356755495E−01
6.446325779E−01	7.730600238E−01	6.770549417E−01
6.547553539E−01	8.778058290E−01	7.137499452E−01
6.441428661E−01	9.673632979E−01	7.544165254E−01
5.580334067E−01	9.880096912E−01	7.329680920E−01
4.839097559E−01	9.937051535E−01	6.583787799E−01
4.517050385E−01	9.957927465E−01	5.616562366E−01
4.498236477E−01	9.968656301E−01	4.580300450E−01

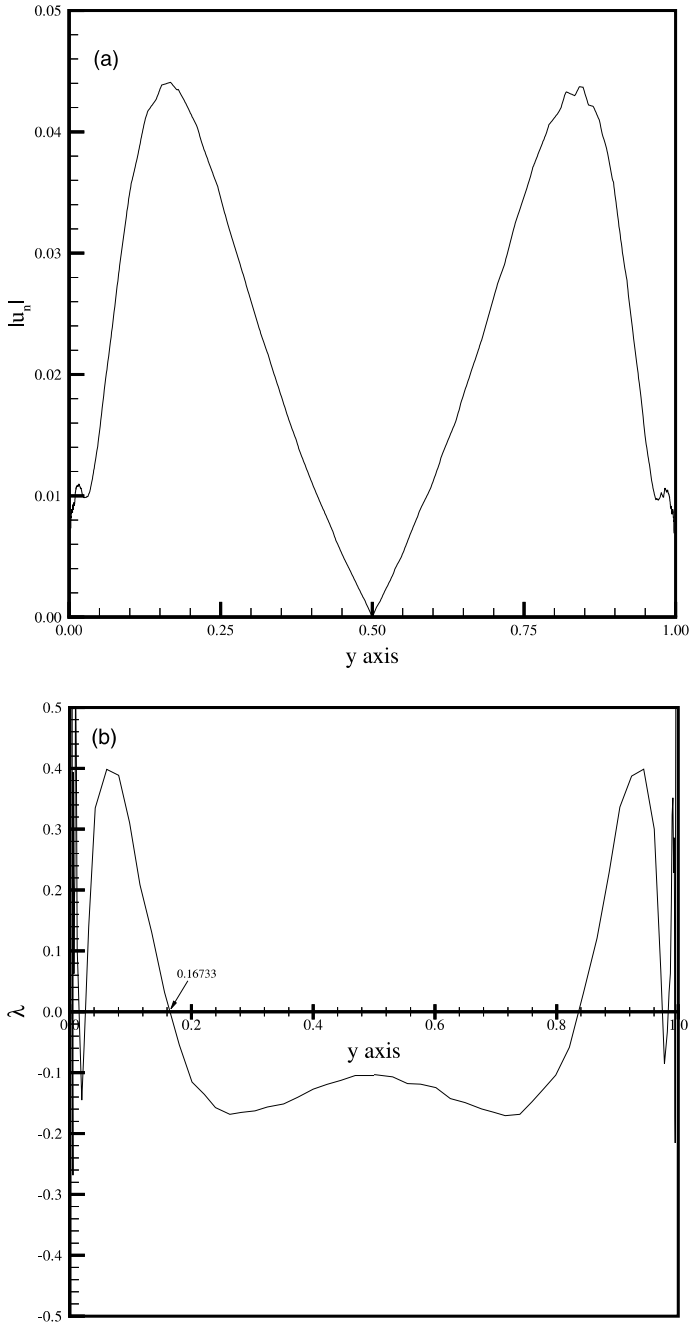

Fig. 10. Velocity component and its derivative against y along the vortical coreline: (a) the distribution of velocity $|u_n|$; (b) the distribution of λ ($\equiv \partial u_n/\partial n$) against y, where n is defined in Fig. 8 or Fig. 9.

to examine if there exists any physically important flow feature that can give us insight into the vortical dynamics.

We can consider an arbitrary plane, schematically shown in Fig. 8. This chosen plane is normal to the vortical coreline at "o" $(0,0,n_0)$. As alluded to earlier, $u_{t_1}(0,0,n_0) = u_{t_2}(0,0,n_0) = 0$. By performing a Taylor series expansion of u_{t_1} and u_{t_2} with respect to "o", we obtain

$$u_{t_1} = \left.\frac{\partial u_{t_1}}{\partial t_1}\right|_0 t_1 + \frac{\partial u_{t_1}}{\partial t_2} t_2 + \cdots, \tag{10}$$

$$u_{t_2} = \left.\frac{\partial u_{t_2}}{\partial t_1}\right|_0 t_1 + \frac{\partial u_{t_2}}{\partial t_2} t_2 + \cdots. \tag{11}$$

Subject to the conservation of mass constraint condition, it is required that the value of λ at point "o" be

$$-\lambda = \left.\frac{\partial u_{t_1}}{\partial t_1}\right|_0 + \left.\frac{\partial u_{t_2}}{\partial t_2}\right|_0. \tag{12}$$

In other words, λ represents the negative of the divergence of the velocity vector at the plane with an outward normal vector n:

$$\Delta = -\lambda. \tag{13}$$

A direct implication of Eq. (12) is that as $\Delta > 0$ (or $\lambda < 0$), the flow decelerates in the direction towards the plane $y = 0.5$. On the other hand, as $\Delta < 0$ (or $\lambda > 0$), the flow keeps accelerating along the vortical coreline in the direction towards the plane of symmetry $y = 0.5$.

We will now focus on the pressure distribution along the vortical coreline by examining the momentum equation along this line. Given that $u_{t_1}|_0 = u_{t_2}|_0 = 0$ along the vortical coreline passing through "o", the resulting equation of motion for particles on this line can be simplified as

$$\Delta = \frac{1}{u_n|_0}\left[\left.\frac{\partial p}{\partial n}\right|_0 - \mu\left(\frac{\partial^2 u_n}{\partial t_1^2} + \frac{\partial^2 u_n}{\partial t_2^2} + \frac{\partial^2 u_n}{\partial n^2}\right)\right]. \tag{14}$$

In the high Reynolds number case (or in the case of a negligibly small value of μ), the sign of Δ depends only on the values of $u_n|_0$ and $(\partial p/\partial n)|_0$. Simple algebraic manipulation leads to the following conclusions: If $u_n|_0 > 0$ and $(\partial p/\partial n)|_0 < 0$, we have $\Delta < 0$ (or $\lambda > 0$) and can have, in turn, an accelerating flow. Otherwise, if $u_n|_0 > 0$ and $(\partial p/\partial n)|_0 > 0$, then $\Delta > 0$ (or $\lambda < 0$) and we have, in turn, a decelerating flow. Along the vortical coreline, we plot in Fig. 11 the computed pressure against the coordinate n. As this figure reveals, the analysis based on the equation of motion in n direction is justified.

In the light of the non-zero values of u_n along the vortical coreline, we were led to expect that fluid particles near "o" would move spirally towards the plane of symmetry. To confirm this, the flow was seeded with markers near two end walls. The result shown in Fig. 12 is a pair of trajectories of massless particles moving under the influence of the spanwise pressure gradient. The sketch of these spirally moving particles raises a question as to the stability of the vortex motions proceeding to the plane of symmetry. To get a theoretical answer to this question, momentum equations are transformed in the coordinate system (t_1, t_2, n). We can then manipulate

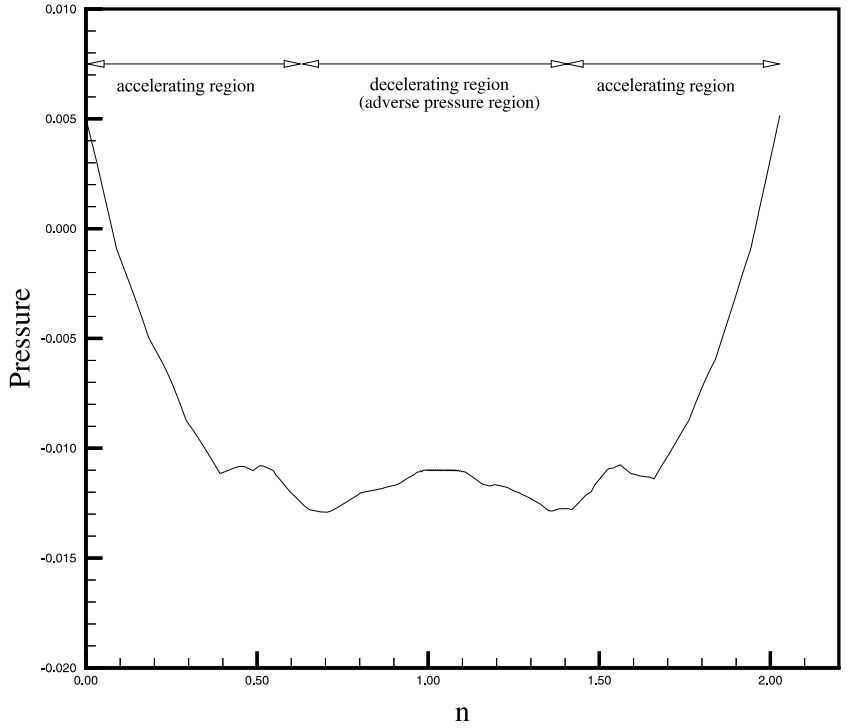

Fig. 11. Pressure distribution against the direction n, as defined in Fig. 8 or Fig. 9, along the vortical coreline.

$\partial/\partial t_1(t_1 - \text{momentum equation}) + \partial/\partial t_2(t_2 - \text{momentum equation}) + \partial/\partial n(n - \text{momentum equation}) = 0$. Let us define the Jacobian of the vector (u_{t_1}, u_{t_2}) as

$$J \equiv \frac{\partial u_{t_1}}{\partial t_1}\bigg|_0 \frac{\partial u_{t_2}}{\partial t_2}\bigg|_0 - \frac{\partial u_{t_1}}{\partial t_2}\bigg|_0 \frac{\partial u_{t_2}}{\partial t_1}\bigg|_0. \tag{15}$$

We can then obtain the following equation for J after some simple algebraic manipulation:

$$J \equiv \Delta^2 + \frac{1}{2}\left(\frac{\partial^2 p}{\partial t_1^2} + \frac{\partial^2 p}{\partial t_2^2} + \frac{\partial^2 p}{\partial n^2}\right). \tag{16}$$

By virtue of Eqs. (14) and (16), the expression for $4J - \Delta^2$ at the point "o" is derived as

$$4J - \Delta^2 = \frac{3}{u_n^2|_0}\left[\frac{\partial p}{\partial n}\bigg|_0 - \mu\left(\frac{\partial^2 u_n}{\partial t_1^2} + \frac{\partial^2 u_n}{\partial t_2^2} + \frac{\partial^2 u_n}{\partial n^2}\right)\bigg|_0\right] + 2\left(\frac{\partial^2 p}{\partial t_1^2} + \frac{\partial^2 p}{\partial t_2^2} + \frac{\partial^2 p}{\partial n^2}\right)\bigg|_0. \tag{17}$$

According to the theorem of ordinary differential equations [42], the necessary condition for a spiralling motion to occur is

$$4J - \Delta^2 = 0. \tag{18}$$

Based on Eq. (17) and the underlying theory leading to Eq. (18), the spiralling motion seen in Fig. 12 is, indeed, physically meaningful. Moreover, according to the Dulac theorem [42], streamlines on the t_1–t_2 plane are of the close-type and are computationally visible in the present study.

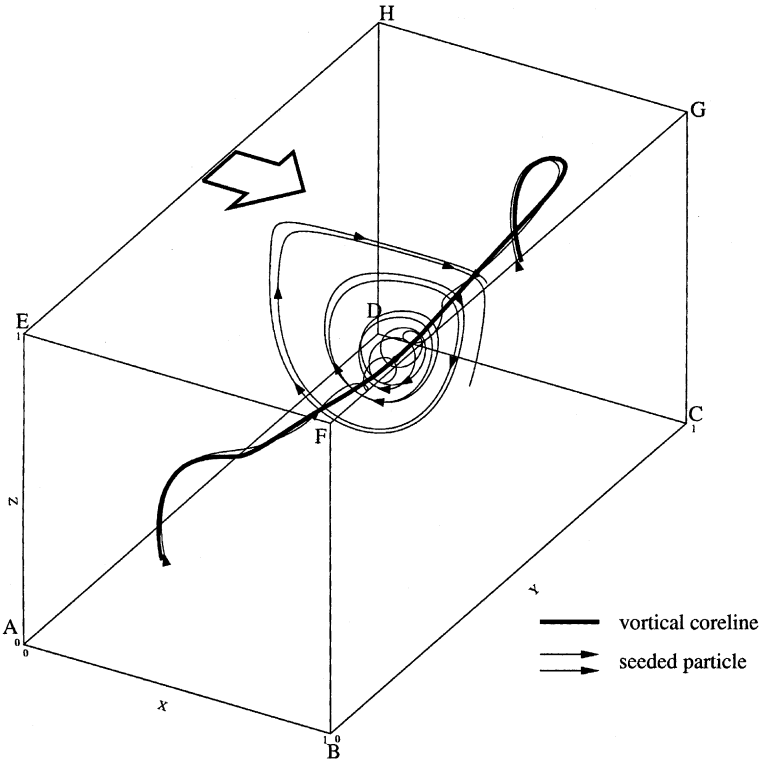

Fig. 12. An illustration of spiralling particle motions about the vortical coreline.

It now remains to investigate the stability of vortical motion for particles moving spirally towards the plane of symmetry. By substituting Eqs. (10) and (11) into $dt_1/dt_2 = u_{t_1}/u_{t_2}$, we can obtain the streamlines on the t_1–t_2 plane:

$$\frac{dt_2}{dt_1} = \frac{(\partial u_{t_2}/\partial t_1)|_0 t_1 + (\partial u_{t_2}/\partial t_2)|_0 t_2}{(\partial u_{t_1}/\partial t_1)|_0 t_1 + (\partial u_{t_1}/\partial t_2)|_0 t_2}. \tag{19}$$

As the flow accelerates towards the plane $y = 0.5$, $\lambda > 0$ (or $\Delta < 0$) can cause a spiralling motion to occur in the vicinity of "o" on the vortical coreline. This motion is stable in the sense that the particles spiral towards "o" (Fig. 13). In contrast to the previous case, as u_n begins decelerating, $\lambda < 0$ (or $\Delta > 0$) destabilizes the spiralling flow motion in view of the particles, seeded immediately adjacent the "o", which repel spirally away (Fig. 14).

4.3. Interior vortex stability and bifurcation

Examining Fig. 10, it is clear to see that $\lambda > 0$ in the range of $0 \leqslant y \leqslant 0.16733$ and $\lambda < 0$ in between $y = 0.16733$ and $y = 0.5$. As a result, at the spatial point $y = 0.16733$, λ is zero along one half of the vortical coreline. The particle which spirals towards the plane of symmetry evolves from the stable vortex region to its unstable counterpart. This finding motivates us to take a closer look at the streamlines on the t_1–t_2 planes, which are adjacent to the point where $\lambda = 0$ along the

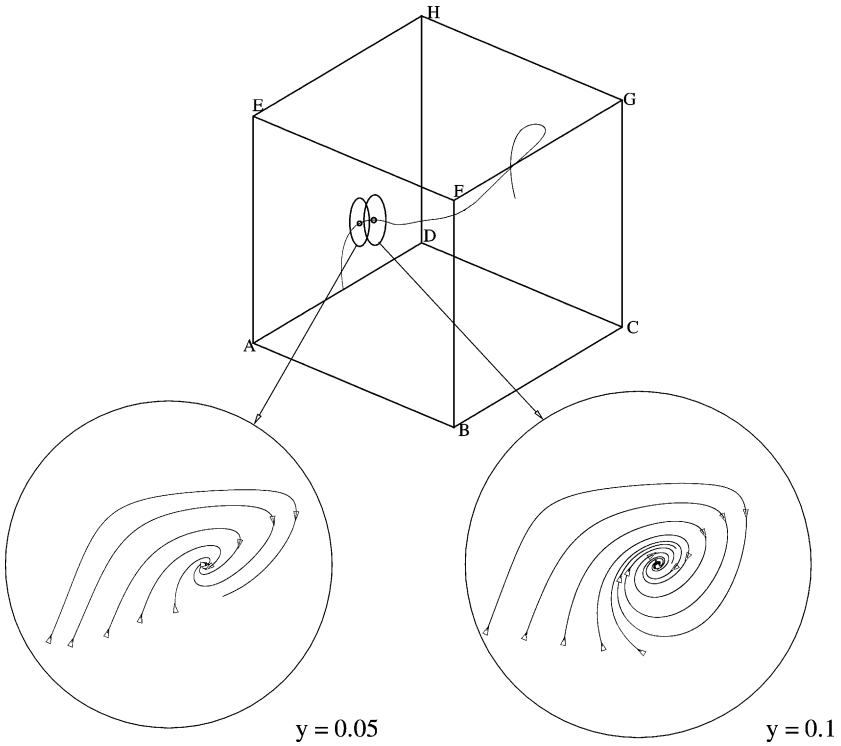

Fig. 13. Particle motions at two cross-flow planes ($y = 0.05$ and 0.1) in the accelerating region.

vortical coreline. We plot in Fig. 15 streamlines on three cutting planes. It is surprising to find that streamlines on planes in between $0.16733 \leqslant y \leqslant 0.3$ exhibit a remarkable change in their vortex orientation in response to the change of sign in λ. Streamlines on the plane immediately downstream of $\lambda = 0$ have two spiralling types. One moves spirally towards the vortical coreline, and the other is repelled spirally away from "o". They have, however, one feature in common in the sense that they both spiral in a clockwise direction. Owing to the inward-and-outward particle motion, we would expect to find a ring, outside of which particles cannot spiral towards the vortical coreline. We call this ring the limiting cycle. On the other hand, particles inside this ring should not be able to spiral outwards. Fig. 15 shows that the inward spiralling flow decreases in size as the flow proceeds toward the plane of symmetry. The implication is that the flow becomes more destabilized as it proceeds toward the plane of symmetry. The limiting cycle schematic in Fig. 15 is stable since λ changes to a negative value from the original positive value. The theoretical proof of this phenomenon has been given by Zhang [43].

We can also apply the topology rule of Hunt et al. [44] to flows on the cross-flow plane to show the validity of the computed solutions from the topological point of view. Take an arbitrary cross-flow plane ($x = 0.634$) as an example; we can determine the critical points of different topological types as shown in Fig. 16. Summing the nodes N, saddles S, half-nodes N', and half-saddles S' reveals that $N = 4$, $S = 1$, $N' = 0$, and $S' = 4$. In the non-obstacle flow interior, these values satisfy the topological rule at the cross-flow plane:

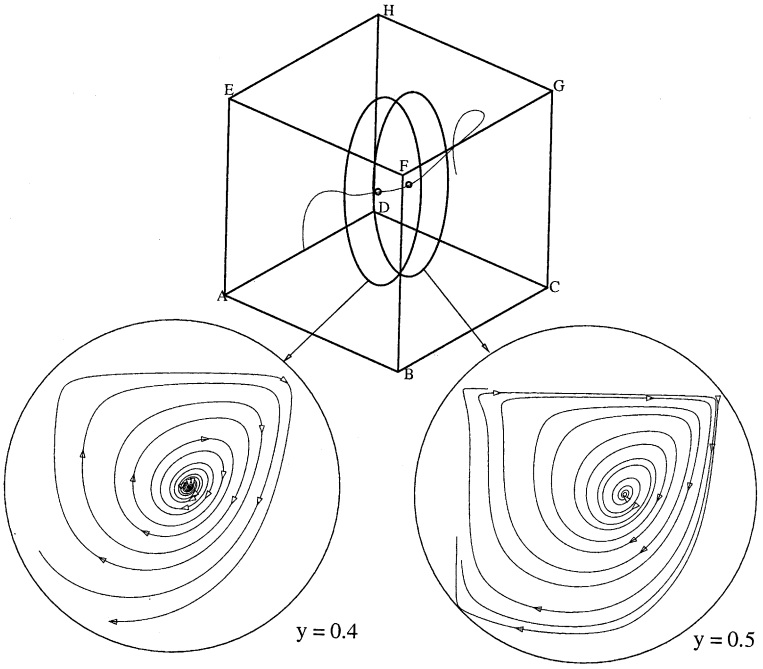

Fig. 14. Particle motions at two cross-flow planes ($y = 0.4$ and 0.495) in the decelerating region.

$$\sum N + \frac{1}{2}\sum N' - \sum S - \frac{1}{2}\sum S' = 1. \tag{20}$$

Here, half-nodes and half-saddles are only seen at two intersecting planes.

This paper will conclude with an investigation of the flow patterns on planes which have stagnation point at the intersection of the vortical coreline and the plane of symmetry. An examination of the streamlines plotted in Fig. 17 reveals that the particles approach this particular singular point from each direction. The adjacent streamlines point towards this saddle point, followed by streamlines repelled away from this point. We will attempt to provide a theoretical justification of the presence of a saddle point on the longitudinal plane. For a point "o" on the vortical coreline, we have, by definition, $u_{t_1} = 0$ and $\partial u_{t_1}/\partial t_2 = 0$. Given that $u_n = 0$ at point "o", we can perform Taylor series expansion on u_{t_1} and u_n as follows:

$$u_{t_1} \approx \left.\frac{\partial u_{t_1}}{\partial t_1}\right|_0 t_1 + \cdots, \tag{21}$$

$$u_n \approx \left.\frac{\partial u_n}{\partial t_1}\right|_0 t_1 + \frac{\partial u_n}{\partial n}|_0 n + \cdots \tag{22}$$

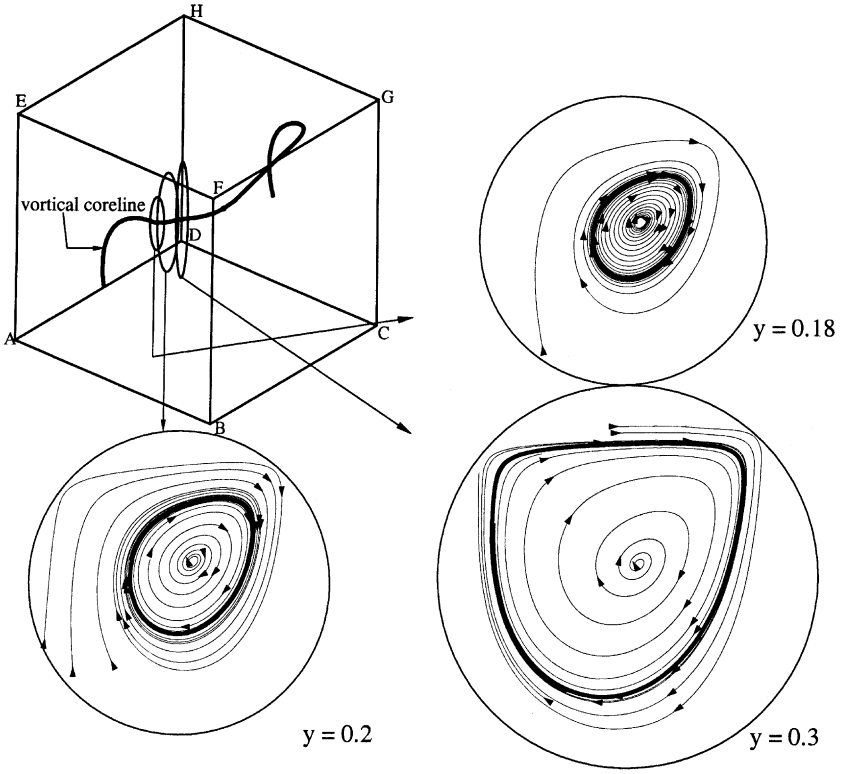

Fig. 15. An illustration of limiting cycles (bold black line, thin line) for showing range of inward/outward spiralling motions at different cross-flow planes $y = 0.18, 0.2$ and 0.3.

Thus, the streamline function on the longitudinal plane is

$$\frac{\partial n}{\partial t_1} \approx \frac{u_n}{u_{t_1}} \approx \frac{(\partial u_n/\partial t_1)|_0 t_1 + (\partial u_n/\partial n)|_0 n}{(\partial u_{t_1}/\partial t_1)|_0 t_1}. \tag{23}$$

Since u_n decreases from a positive value to zero at "o", $(\partial u_n/\partial n)|_0 < 0$ and $\lambda < 0$ result. The consequence of the negative value of λ is that the streamline beginning at "o" on the vortical coreline is repelled outwards. This implies that $(\partial u_{t_1}/\partial t_1)|_0 > 0$ and, thus, $J(\equiv (\partial u_{t_1}/\partial t_1)|_0 (\partial u_n/\partial n)|_0) < 0$ in the vicinity of the stagnation point. As a result, the streamline on the longitudinal plane is of the saddle-type.

5. Concluding remarks

We have presented three-dimensional computations of steady-state incompressible Navier–Stokes equations. The results were obtained based on the streamline upwind finite element model, implemented on quadratic elements to avoid cross-wind diffusion errors. In the present three-dimensional mixed finite element model, we have used the BiCGSTAB to solve large-size unsymmetric and indefinite matrix equations. This iterative solver has been implemented in an

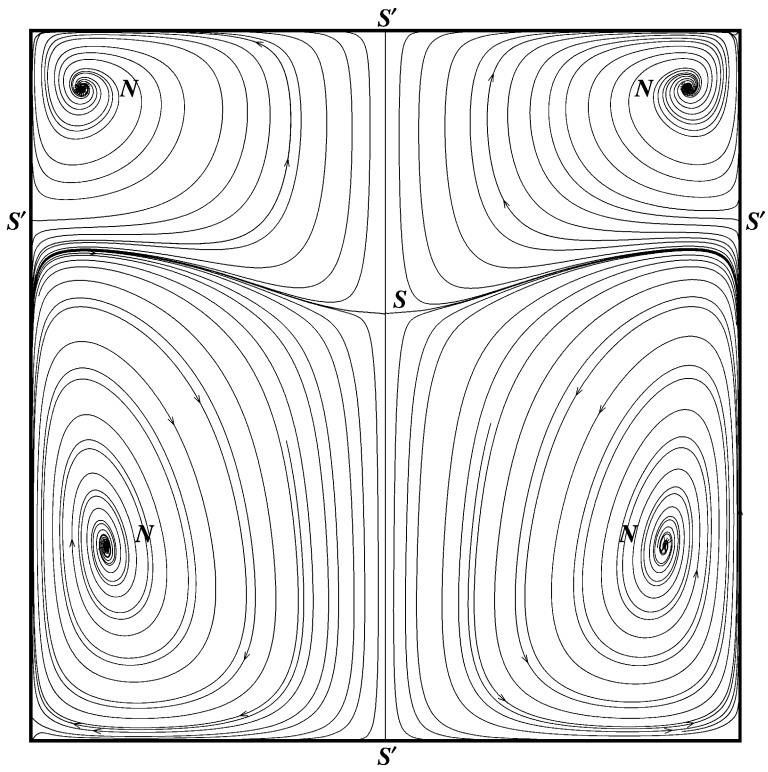

Fig. 16. Streamlines and critical points plotted at the cross-flow plane $x = 0.634$.

element-by-element format to improve the computational performance. To explore the flow, we have adopted a theoretically rigorous theory of topology on the velocity vector field. In this study, we have considered limiting streamlines immediately above the wall surface. Since the kinematic nature of these limiting streamlines is best described by singular points, we have determined them and plotted nodes, foci, and saddles on the no-slip walls and have theoretically justified their presence. Streamlines on both the cross-flow and longitudinal planes have also been investigated, with emphasis placed on the flow pattern in the vicinity of the vortical coreline. In the cavity, longitudinal vortices originating from regions near the two vertical end walls spiral towards the plane of symmetry. In the beginning of these vortex motions, they are affected by a favored pressure gradient and are, thus, classified as being stable along the vortical coreline. In its approach to the plane of symmetry, the adverse pressure causes the velocity component tangential to the vortical coreline to decrease. The flow in such an adverse pressure gradient region is, thus, less stable. As the velocity that is tangential to the vortical coreline decreases, a stable limiting cycle is found in the streamlines plotted on the downstream cross-flow planes. This so-called limiting cycle can divide streamlines into two groups. In the outer one, streamlines spiral towards the vortical coreline. In contrast with this outer spiralling motion, streamlines inside the limiting cycle tend to spiral outwards and, thus, to destabilize the longitudinal vortex motion. Such a destabilized vortex convects downstream in the adverse pressure gradient region and can lead to flow unsteadiness in the form of a Hopf bifurcation as the Reynolds number keeps

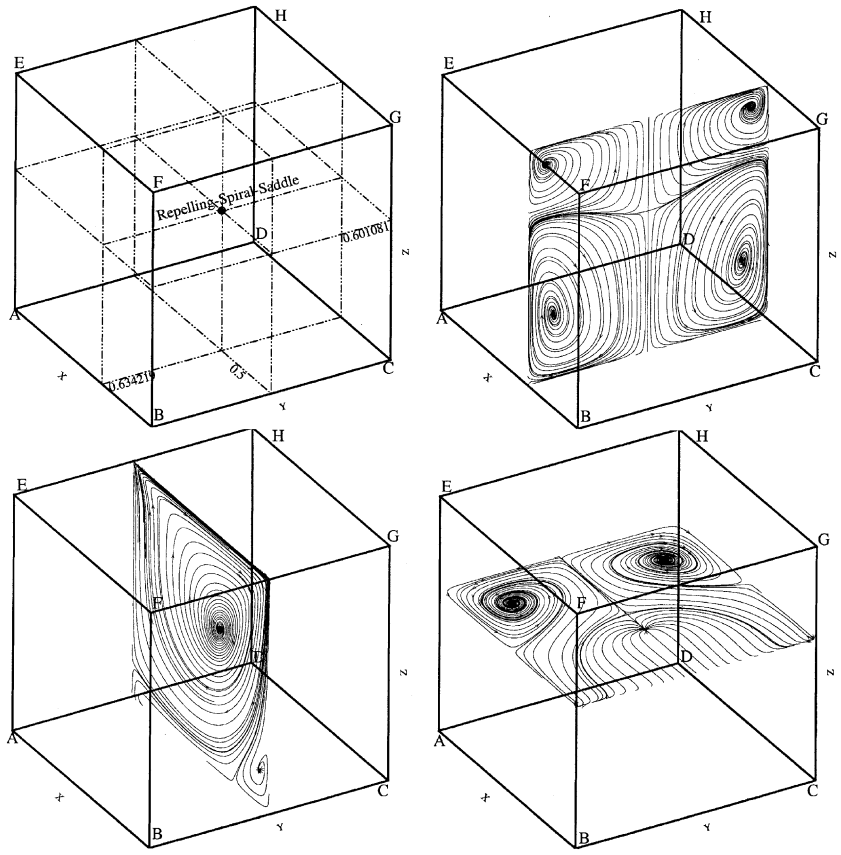

Fig. 17. Streamlines plotted at planes which pass the stagnation point on the vortical coreline.

increasing. On the longitudinal plane near the plane of symmetry, the flow pattern has saddle-type streamlines.

Acknowledgements

Financial support from the National Science Council of the Republic of China under Grant NSC-84-2212-E-002-060 is gratefully acknowledged. The authors also thank the Computer Center of National Taiwan University and the National Center of High-performance Computing (NCHC) for providing parallel computers.

Appendix A

Referring to Fig. 5, the definition of singular point demands $(\partial v/\partial z|_0) = 0$. According to Eq. (9), the limiting streamline passing over the point "o" can be further simplified as

$$\frac{\mathrm{d}x}{\mathrm{d}y} = \frac{(\partial^2 u/\partial x\,\partial z)|_0 x}{(\partial^2 v/\partial x\,\partial z)|_0 x + (\partial^2 v/\partial y\,\partial z)|_0 y}. \tag{A.1}$$

Without loss of generality, $(x, y) = (0, y_s)$ is assumed to be a singular point on the line of separation. Introducing the following auxiliary transformation

$$\xi = x, \tag{A.2}$$

$$\eta = y - y_s, \tag{A.3}$$

one can express Eq. (A.1) as

$$\frac{\mathrm{d}\eta}{\mathrm{d}\xi} = \frac{(\partial^2 v/\partial y\,\partial z)|_s\,\eta}{(\partial^2 u/\partial x\,\partial z)|_s\,\xi}. \tag{A.4}$$

By virtue of Eq. (7), we can have $(\partial^2 u/\partial x\,\partial z)|_s < 0$. According to the definition of singular point, we have $(\partial u/\partial z)|_s = 0$. Since point "o" is away from the point "s" with a fairly short distance, it is rational to conclude that $(\partial v/\partial z)|_0 > 0$. As a result, the classification of singular point depends on the sign of $(\partial^2 v/\partial z^2)|_s$. If $\partial^2 v/\partial z^2 > 0$, it follows that $\mathrm{d}\eta/\mathrm{d}\xi < 0$. This implies that the singular point at $(0, y_s)$ must be a saddle. On the other hand, if $\partial^2 v/\partial z^2 < 0$, we have $\mathrm{d}\eta/\mathrm{d}\xi > 0$ and the singular point $(0, y_s)$ is referred to as a node.

References

[1] Pan F, Acrivos A. Steady flows in rectangular cavities. J Fluid Mech 1967;28:643–55.
[2] Bogatyrev VY, Gorin AV. End effects in rectangular cavities. Fluids Mech—Soviet Res 1978;7(4):101–6.
[3] Koseff JR, Street RL, Gresho PM, Upson CD, Humphrey JAC, To WM. A three-dimensional lid-driven cavity flow: experiment and simulation. In: Johnson JA, Taylor C, Smith WR, editors. Numerical methods in laminar and turbulent flows. Swansea, UK: Pineridge Press; 1983. p. 564–81.
[4] Koseff JR, Street RL. Visualization studies of a shear driven three-dimensional recirculating flow. ASME J Fluids Eng 1984;106:21–9.
[5] Koseff JR, Street RL. On end wall effects in a lid-driven cavity flow. ASME J Fluids Eng 1984;106:385–9.
[6] Koseff JR, Street RL. The lid-driven cavity flow: a synthesis of qualitative and quantitative observations. ASME J Fluids Eng 1984;106:390–8.
[7] Prasad AK, Koseff JR. Reynolds number and end-wall effects on a lid-driven cavity flow. Phys Fluids 1989;1:208–18.
[8] Aidun CK, Triantafillopoulos NG, Benson JD. Global stability of a lid-driven cavity with through flow: flow visualization studies. Phys Fluids 1991;3:2081–91.
[9] Koseff JR, Street RL. Visualisation studies of a shear driven three dimensional fiow. In: Three-Dimensional Turbulent Shear Driven Flows. New York: ASME; 1982. p. 23–31.
[10] Freitas CJ, Street RL, Findikakis AN, Koseff JR. Numerical simulation of three-dimensional flow in a cavity. Int J Numer Meth Fluids 1985;5:561–75.
[11] Freitas CJ, Street RL. Non-linear transport phenomena in a complex recirculating flow: a numerical investigation. Int J Numer Meth Fluids 1988;8:769–802.
[12] Perng CY, Street RL. Three-dimensional unsteady flow simulations: alternative strategies for a volume-averaged calculation. Int J Numer Meth Fluids 1989;9:341–62.
[13] Zang Y, Street RL, Koseff JR. A non-staggered grid, fractional step method for time-dependent incompressible Navier–Stokes equations in curvilinear coordinates. J Comp Phys 1994;114:18–33.
[14] Burggraf OR. Analytical and numerical studies of the structure of steady separated flows. J Fluid Mech 1966;24:113–51.

[15] Shankar PN, Deshpande MD. Fluid mechanics in the driven cavity. Annu Rev Fluid Mech 2000;32:93–136.
[16] Deville M, Lê TH, Morchoisne Y. Numerical simulation of 3-D incompressible unsteady viscous laminar flows. In: Notes on Numerical Fluids Mechanics, A GAMM-Workshop, vol. 36, 1992. p. 73–89.
[17] Chiang TP, Hwang RR, Sheu WH. Finite volume analysis of spiral motion in a rectangular lid-driven cavity. Int J Numer Meth Fluids 1996;23:1–22.
[18] Chiang TP, Hwang RR, Sheu WH. On end-wall corner vortices in a lid-driven cavity. ASME, J Fluids Eng 1997;119:201–4.
[19] Chiang TP, Sheu WH, Hwang RR. Three-dimensional vortex dynamics in a shear-driven rectangular cavity. J Comp Fluid Dyn 1997;8:201–14.
[20] Chiang TP, Sheu WH. Numerical prediction of eddy structure in a shear-driven cavity. J Comp Mech 1997;20: 379–96.
[21] Chiang TP, Sheu WH, Hwang RR. Effect of Reynolds number on the eddy structure in a shear-driven cavity. Int J Numer Meth Fluids 1998;26:557–79.
[22] Legendre R. Séparation de courant Íéconlment laminaire tridimensional. Rech Aéro 1956;54:3–8.
[23] Levy Y, Degani D, Seginer A. Graphical visulization of vortical flows by means of helicity. AIAA J 1990; 28(8):1347–52.
[24] Lighthill MJ. Attachment and separation in three-dimensional flow. In: Rosenhead L, editor. Laminar Boundary Layers, vol. 2.6. Oxford: Oxford University Press; 1963, p. 72–82.
[25] Gunzburger MD. Finite element methods for viscous incompressible flows, a guide to theory, practice, and algorithms. London: Academic Press; 1989.
[26] Babuška I. Error bounds for finite element methods. Numer Math 1971;16:322–33.
[27] Brezzi F, Douglas J. Stabilized mixed methods for the Stokes problem. Numer Math 1988;53:225–35.
[28] Sheu TWH, Wang MMT, Tsai SF. Element by element parallel computation of incompressible Navier–Stokes equations in three dimensions. SIAM J Sci Comput 2000;21(4):1387–400.
[29] Van der Vorst HA. BI-CGSTAB: a fast and smoothly converging variant of BI-CG for the solution of nonsymmetric linear systems. SIAM J Sci Statist Comput 1992;13(2):631–44.
[30] Ladyzhenskaya OA. Mathematical problems in the dynamics of a viscous incompressible flow. New York: Gordon and Breach; 1963.
[31] Hughes TJR. Finite element methods for convection dominated flows, AMD. New York: ASME; 1979.
[32] Patankar SV. Numerical heat transfer and fluid flow. Washington, DC: Hemisphere; 1980.
[33] Varga RS. Matrix iterative analysis. Englewoodcliff, NJ: Prentice-Hall; 1962.
[34] Fletcher R. Conjugate gradient methods for indefinite systems. In: Lecture Notes in Mathematics, vol. 506. Berlin: Springer; 1976. p. 73–89.
[35] Wang MMT, Sheu TWH. An element-by-element BiCGSTAB iterative method for three-dimensional steady Navier–Stokes equations. J Comp Appl Math 1997;79:147–65.
[36] Babu V, Korpela SA. Numerical solution of the incompressible three-dimensional Navier–Stokes equations. Comput Fluids 1994;23(5):675–91.
[37] Kato Y, Kawai H, Tanahashi T. Numerical flow analysis in a cubic cavity by the GSMAC finite-element method. JSME Int J Series II 1990;33:649–58.
[38] Davey A. Boundary-layer flow at a saddle point of attachment. J Fluid Mech 1961;10(4):593–610.
[39] Zhang H. The separation criteria and flow behavior for three-dimensional steady flow. ACTA Aerodynamica Sinica 1985;1:1–12.
[40] Zhang H, Deng X. Analytic studies for three dimensional steady separated flows and vortex motion. ACTA Aerodynamica Sinica 1992;10(1):8–19.
[41] Wang KC. Boundary-layer over a blunt body at low incidence with circumferential reversed flow. J Fluid Mech 1975;72(1):49–65.
[42] Jordan DW, Smith P. Nonlinear ordinary differential equations. Oxford: Clarendon Press; 1977.
[43] Zhang H. Bifurcation of vortex motion along its axis. ACTA Aerodynamica Sinica 1994;12(3):243–51.
[44] Hunt JCR, Abell CJ, Peterka JA, Woo H. Kinematical studies of the flows around free or surface-mounted obstacles; applying topology to flow visualization. J Fluid Mech 1978;86:179–200.